Journal of Alzheimer's Disease 33 (2013) 165–176
DOI 10.3233/JAD-2012-120745
IOS Press



# Spatiotemporal Complexity of Fibroblast Networks Screens for Alzheimer's Disease

Florin V. Chirila, Tapan K. Khan* and Daniel L. Alkon
*Blanchette Rockefeller Neurosciences Institute, Morgantown, WV, USA*

Accepted 18 July 2012

**Abstract**. Drugs to treat Alzheimer's disease (AD) have been unsuccessful in preventing its devastating cognitive deficits and progressive neurodegeneration. The lack of a definitive diagnostic for AD has been a major obstacle to AD drug discovery. Here, we describe a novel, highly accurate peripheral diagnostic for AD patients based on quantitatively measured complexity of skin-sampled fibroblast networks. A significant number of samples were studied under double-blind conditions and had autopsy and/or genetic validation. An additional sample confirmed the diagnostic discrimination on freshly obtained skin samples. A subsample of these diagnostic differences were induced by oligomerized amyloid-$\beta_{1\text{-}42}$. Based on the accuracy of these measures that utilize physical principles such as fractal dimension and lacunarity as well as the significant correlation with disease duration, this biomarker profile appears to identify accurately AD patients for therapeutic intervention.

Keywords: Alzheimer disease, biomarkers, cell aggregation, cell migration, diagnosis, fractal dimension, lacunarity, networks

Supplementary data available online: http://www.j-alz.com/issues/33/vol33-1.html#supplementarydata04

## INTRODUCTION

The complexity of Alzheimer's disease (AD) raises a great challenge for early screening. A biological marker that would predict AD prior to symptomatic diagnosis and/or definitively diagnose early AD could have a major impact in testing and treating AD in our growing elderly population. The long term prodromal stages, co-morbidity with other non-Alzheimer's disease dementia (non-ADD), and the multi-factorial nature of AD offer further challenges for successful diagnosis with a single biological marker.

Accumulating evidence indicates that AD can cause pathophysiological changes not only in the central nervous system (CNS), but also in peripheral tissues. AD metabolic pathways are ubiquitous in the human body and are found in blood [1–4], saliva [5, 6], skin fibroblasts [7–10], or in the human lens [11]. Diagnosing and testing pathophysiological hypotheses for AD in peripheral tissue are potentially minimally invasive, cost-effective, and much more readily accessible, when compared with CNS biomarkers.

Candidate fibroblasts biomarkers for AD have been based on K+ channels [12, 13], protein kinase C (PKC) isozymes [14, 15], $Ca^{2+}$ signaling components [16], MAP kinase extracellular regulated kinase 1/2 (ERK 1/2) phosphorylation [17], bradykinin-induced phosphorylation of ERK1 and ERK2 [18, 19], mitochondrial function [20], antioxidative pathway components [21], and bradykinin activity [22]. Abnormal changes in membrane fluidity [23, 24], changes in cytoskeletal proteins expressions [25, 26], and decreased adhesiveness [27] in AD fibroblasts were also reported. The extracellular matrix, a complex network composed of an array of macromolecules important for regulation of cell functions and tissue architecture, is dysregulated in AD skin fibroblasts

*Correspondence to: Tapan K. Khan, Blanchette Rockefeller Neurosciences Institute, 8 Medical Center Drive, Morgantown, WV 26506, USA. Tel.: +1 304 293 0934; Fax: +1 304 293 3675; E-mail: tapan_khan@brni-jhu.org.

ISSN 1387-2877/13/$27.50 

[28]. The microtubule networks are disrupted in familial AD patients when compared with age-matched controls [29].

The multitude of previously implicated pathways in AD fibroblasts emphasizes the complexity of this disease. These pathways are very likely interconnected in a complex network-like structure. Therefore, we were interested from the diagnostic point of view to capture this complexity with integrative and dynamic measures of network complexity such as fractal dimension and lacunarity. The complexity of actually interconnected pathways suggested a novel approach to AD screening based on a collection of markers rather than just one.

For these reasons we quantitatively discriminated the dynamics of AD fibroblast network formation in culture conditions from age-matched control (AC) cases and non-ADD patients. The four markers described here quantitatively assess patterns of fibroblast network dynamics on a three dimension (3-D) matrix.

## MATERIALS AND METHODS

### *Banked and fresh cell lines used in this study*

We carried out experiments using skin fibroblast samples from 33 patients as provided by the Coriell Institute for Medical Research (Camden, NJ), (Table 1 and Supplementary Table 1; available online: http://www.j-alz.com/issues/33/vol33-1.html#supplementarydata04) and plated them on a thick layer (∼1.8 mm) of 3-D matrix (Matrigel, BD Biosciences, San Jose, CA) on 12 well plates. The available patient information is posted on Coriell web site (http://ccr.coriell.org/) and is now summarized in detail in Supplementary Table 1. The cell lines analyzed (33) were, for the most part (30/33) very well characterized based on a number of criteria: autopsy and genetic family history (Table 1). A significant number of samples ($n = 13$) were studied under double-blind conditions, and a further sample confirmed the diagnostic differentiation on freshly obtained skin samples (green symbols in Fig. 1D). The age-matched control cells chosen for this paper were not demented at the date of skin biopsy extraction. All the samples were taken antemortem with two exceptions, AG05770 and AG08245, which were taken postmortem. The banked skin fibroblast cells were frozen stocks under liquid nitrogen. Primary cultures were established after thawing those frozen samples and followed through successive passaging [17–19]. All cell lines used in this study, were primary cell lines and were not treated in order to be immortalized.

Freshly taken fibroblasts were obtained as follows. Punch-biopsies (2-3 mm, upper arm) skin tissues from patients and controls were obtained by qualified personnel under the supervision of Dr. Shirley Neitch with the IRB approval of Marshall University (Huntington, WV). All patients (or relatives/representatives) signed informed consent forms. The clinical diagnosis was conducted by Dr. Neitch. The Institutional Review Board at Marshall University approved the procedure. The method of isolating fibroblasts from skin biopsies was followed as described elsewhere [17]. For the tests described here, we used cells with passages between 5 and 15.

The initial cell density was controlled to be 50 cells/mm$^3$ and was homogenized with 1.5 ml Dulbecco's Modified Eagle Medium with 10% fetal bovine serum and 1% penicillin/streptomycin for each well. Cells were kept in a $CO_2$ water-jacket incubator (Forma Scientific) up to 7 days after plating.

### *Image capture*

Images of the cellular networks were captured with an inverted microscope (Westover Digital AMID

Table 1
Banked cell lines used in this study

| Diagnostic criteria | Rule AD IN | Rule AD OUT | | Total |
|---|---|---|---|---|
| | AD patients | Non-ADD | Non-demented controls | |
| Autopsy confirmed | 7 | 1 PD | – | |
| Genetic & family history | 3 | 7HD+1PD | – | |
| Clinical diagnosis ONLY | 3 | – | – | |
| Total | 13 | 9 | 11 AC | 33 |
| Well characterized | **10** | **9** | **11** | **30** |

AC-Age-matched controls; HD-Huntington's disease; AD-Alzheimer's disease; PD-Parkinson's disease.

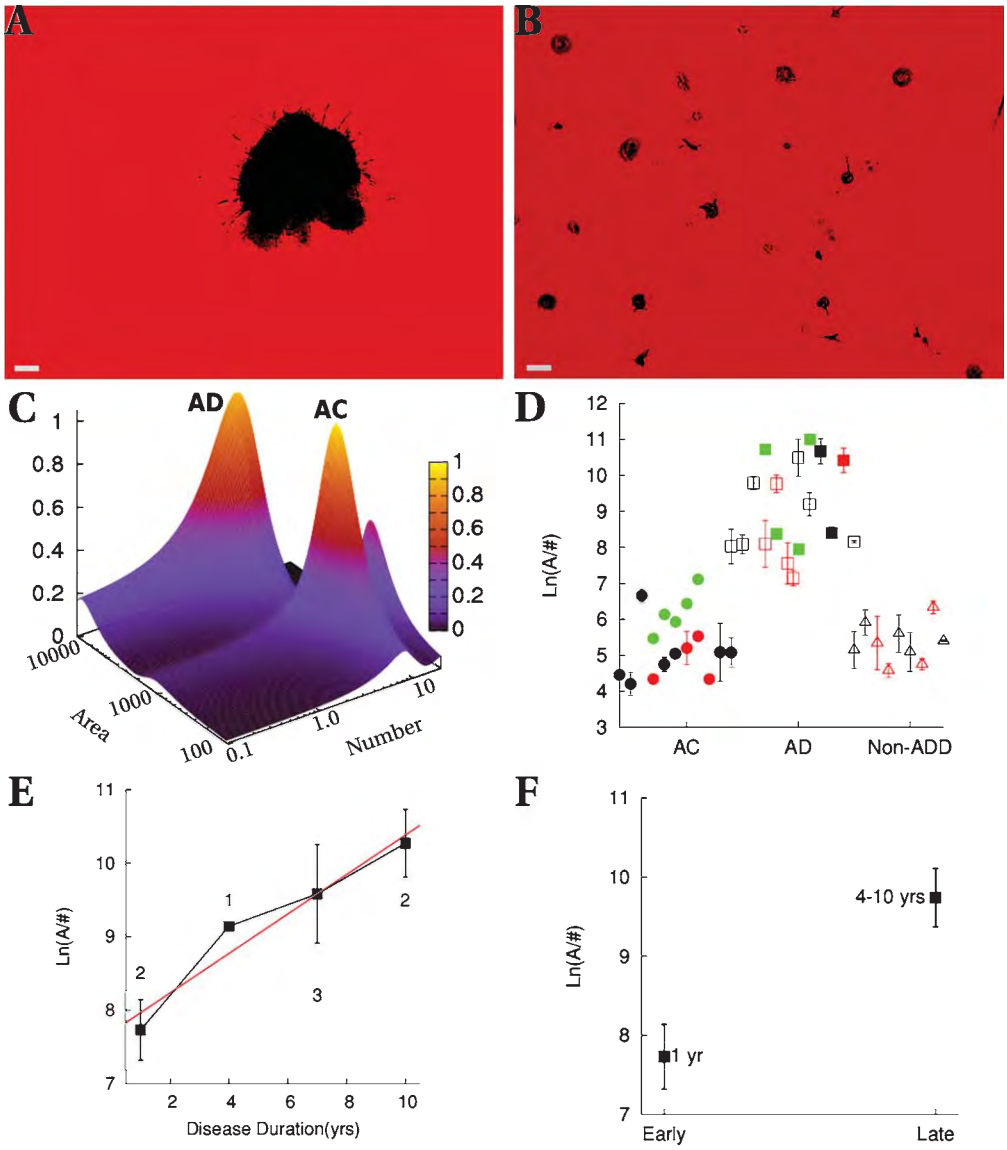


Fig. 1. Measure I: Area per number of aggregates. Examples of Alzheimer's disease (AD) fibroblasts aggregates (A), and age-matched controls (AC) (B) at 48 h (see Materials and Methods section for details). Scale bar is 10 μm. C) Probability distribution of cellular aggregates as a function of area and number at 48 h. The AD group ($n = 13$) separated well from the AC group ($n = 11$). D) Population data for the measure of natural logarithm of the ratios of aggregate areas to their number, Ln(Area/#), for AC ($n = 11$; circles), AD ($n = 13$; squares), non-ADD ($n = 9$; triangles). Empty symbols represent autopsy or genetic validated samples, while red represent samples analyzed under double-blind conditions. Green symbols represent fresh samples. E) Increase of area per number of aggregates with disease duration. Numbers associated with each point represent the number of cell lines. Red line is the best linear fit for the duration points. F) Measurements for the 1 year disease duration ($n = 2$) were markedly lower than the measures for ≥4 years of disease duration ($n = 6$). Ln(Area/#) was significantly smaller ($p < 0.039$) than the late measure. Error-bars represent the standard error of the mean (SEM).

Model 2000, Westover Scientific, Bothell WA), controlled by a computer via an image acquisition software (Micron 2.0.0), using a 10× and a 4× objective. We captured five images per well and typically we used three wells per cell line. In the first day we acquired images every hour, the second day every other hour, and for the remaining three days we acquired images three times a day. Images were processed with ImageJ, a freely available software from NIH (http://rsbweb.nih.gov/ij/).

*Image acquisition and quantification*

The 5 images per well were initially taken using the same standard pattern, center (1), up (2), down (3), left (4), right (5), by moving one field with respect to the central image (Supplementary Figure 1). Later in the process, we increased the number of images from 5 to 9 by filling the corners of the rectangle with images from 6 to 9 (dotted lines in Supplementary Figure 1), in order to increase the area investigated and further improve the coefficient of variation without affecting the diagnostic discriminability. Image 1 was always in the center of the well. To determine the center of the well we used one of the following methods: a) the live image under 4× magnification should be symmetric, i.e., the shadows in the four corners should have equal areas for an aligned microscope; b) mark the center with a needle; or c) use gridded plates (Pioneer Scientific; Shrewsbury, MA) where the central square is always the 6th, in the central row or column. For image quantification we used two sets of tools: initially manual as provided by Micron, software which came with the microscope; later automated with ImageJ.

For the initial cell count, we used a custom ImageJ plug-in in which we ran "despeckle" three times; we then filtered the image three times with a minimum filter of radius 0.5; and then we ran "Subtract Background" with a rolling radius of 20. Finally, we made the image binary and ran "Analyze Particles" in the size range 180-Infinity. All of these ImageJ commands were run inside a loop so that we could analyze all the images from one cell line automatically. The ImageJ plug-in was tuned by using manual cell counts on the same images and the relative error was below 7%.

The target number of cells per 10× image was 417 which corresponded to an initial cell concentration of 50 cells/μl (Supplementary Figure 3B). We allowed a variation of cell concentration between 45 and 60 cells/μl. To minimize heterogeneity of the cell distribution in the image, we eliminated images outside of the range 195–650 cells per 10× image.

For cellular aggregates at 48 h we used manual ellipse fitting with the Micron software.

*Fractal dimension and lacunarity*

For fractal and lacunarity analyzes we used the FracLac_2.5 plug-in (http://rsbweb.nih.gov/ij/plugins/fraclac/fraclac.html) using the "box counting" method [30–33]. The recovery slope and intercept was monitored by fitting a line (See Data analysis section and Fig. 2C-pink line) in the range 20–80% of the min-max difference. The average lacunarity was calculated between 0 and 120 h.

*Average area per number of aggregates*

Average area per number of aggregates was calculated in the following manner. For each image we calculate an average aggregate area $<A>_i$ and a number of aggregates $N_i$. Then for each image we evaluate the ratio $<A>_i/N_i$. Typically, we used five images per well and we evaluate an average area per number for each well as $\frac{1}{5}\sum_{i=1}^{5}\frac{\langle A\rangle_i}{N_i}$. Then we average once more over the three wells $\frac{1}{3}\sum_{w=1}^{3}\left(\frac{1}{5}\sum_{i=1}^{5}\frac{\langle A\rangle_i}{N_i}\right)_w$. Then the natural logarithm of this measure, $\ln\left(\frac{1}{3}\sum_{w=1}^{3}\left(\frac{1}{5}\sum_{i=1}^{5}\frac{\langle A\rangle_i}{N_i}\right)_w\right)$, was calculated for each cell line (Fig. 1D). The aggregates were manually fitted with ellipses using Micron 2.0 software and their area and number were recorded. We developed an automatic script for ImageJ which agrees well with manual ellipse fitting. These two approaches were within one standard deviation of each other.

*Cell migration*

Freely migrating cells were counted at 48 h, $N_1$, and approximately 7 h later, $N_2$. The migration rate was calculated as $R = (N_2 - N_1)/\Delta T$, where $\Delta T$ is the time interval between counts.

*Effect of amyloid-β (Aβ) on network formation, cellular aggregation, and migration*

AC and AD fibroblasts were treated overnight in T25 flasks with 1 μM oligomerized Aβ; then cells were plated on 3-D matrix using the same cell density 50 cells/mm$^3$. We used the same four measures of the network: cellular aggregation at 48 h after plating, fractal and lacunarity curves, and cellular migration.

*Preparation of oligomerized Aβ*

Oligomerized Aβ was prepared by a method adapted from Hoshi et al., Noguchi et al., and Sen et al. [34–36]. Briefly, $Aβ_{1\text{-}42}$ was dissolved in 1,1,1,3,3,3-hexafluoro-2-propanol and incubated overnight at 4°C and then for 3 h at 37°C. Finally, the dissolved $Aβ_{1\text{-}42}$ was lyophilized in 1.5-ml polypropylene centrifuge tubes at 40 nM/tube concentration. For preparing the

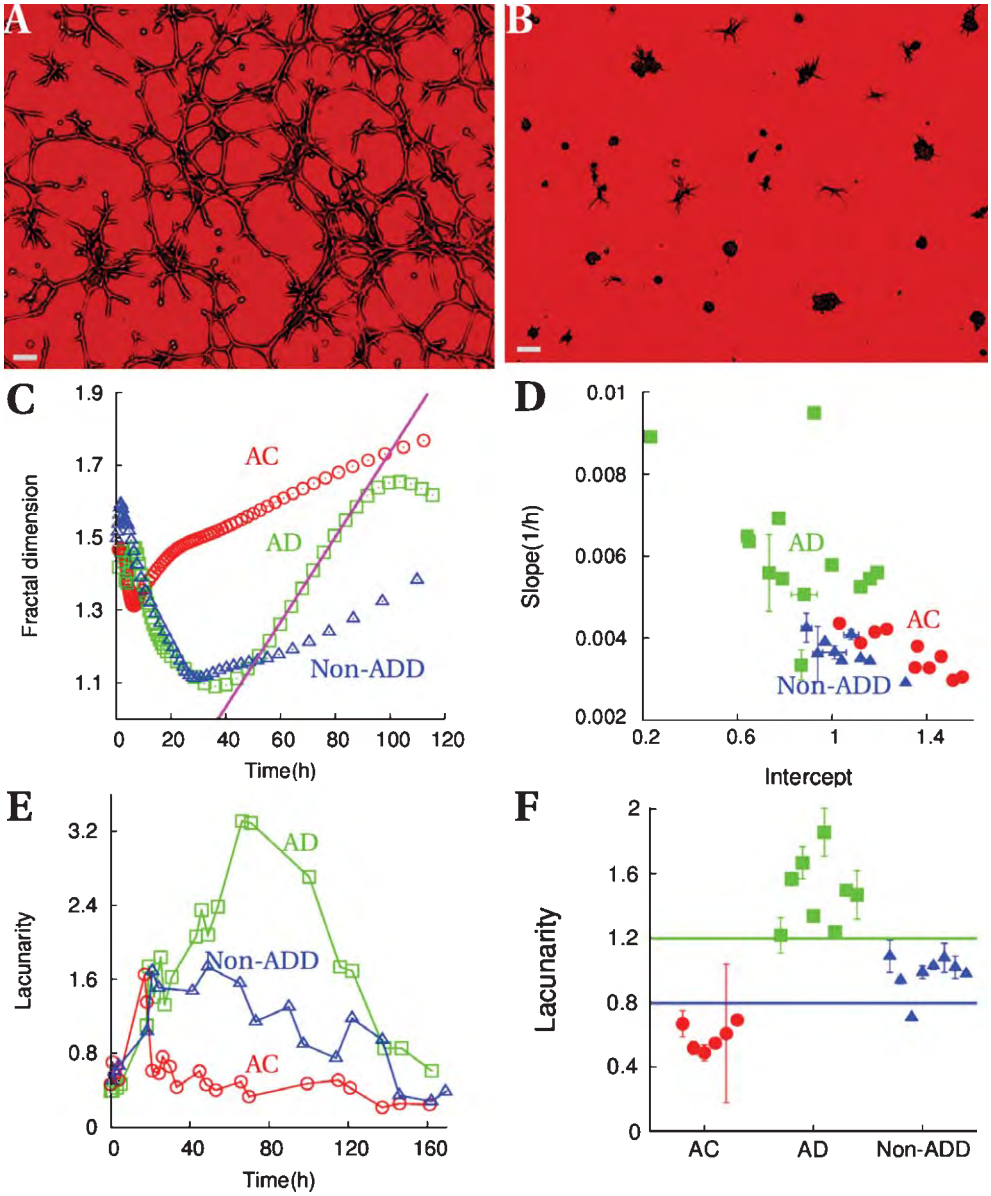


Fig. 2. Measures II and III. Fractal and lacunarity analyses. One hour after incubation, the fractal dimension for this AC cell line was 1.72 (A) and lacunarity is 0.37, while after 48 h the fractal dimension dropped to 1.05 and lacunarity increases to 0.75 (B). Scale bar is 10 μm. C) Examples of fractal curves for one AD, one AC, and one non-ADD cases. The recovery slope and intercept was monitored by fitting a line (pink) in the range 20–80% of the min-max difference. D) Population data for slope versus intercept of the recovery for fractal curves: AD-green ($n = 13$), AC-red ($n = 10$), non-ADD-blue ($n = 9$). E) Examples of lacunarity curves for AD, AC, and non-ADD. F) The average lacunarity was used as a measure for separating the three groups: AD-green ($n = 8$, square), AC ($n = 6$, red), non-ADD ($n = 8$, blue). Error-bars are standard errors of the means (SEM).

oligomerized Aβ, the lyophilized Aβ was dissolved in phosphate-buffered saline (PBS) without $Ca^{2+}$ or $Mg^{2+}$ at less than 50 mM concentration and rotated for 14 h at 4°C. After incubation, the Aβ solution was purified using a 0.65 μm cut-off filter (Amicon Ultra, Millipore) to remove the fibrils, and the soluble fraction was saved to obtain the most toxic oligomers. The sizes of the oligomers were determined by size exclusion chromatography and atomic force microscopy in our laboratory and found to be oligomeric. Atomic force microscopy studies showed that the majority of the species were ∼8–10 nm in height consistent with the

previous findings [36]. Before treatment of the fibroblasts, the toxicity of the Aβ oligomers was regularly checked by standard neurotoxicity assays [36].

*Data analysis*

For data analysis we used Gnuplot 4.4, a freely available software (http://www.gnuplot.info). For fitting of the raw data points, we used a built in fit function from Gnuplot, which uses an implementation of the nonlinear least-squares (NLLS) Marquardt-Levenberg algorithm. Unless otherwise specified, the error-bars are standard errors of the mean (SEM).

*Probability distribution of cellular aggregates*

For all the AD and all the AC patients, we binned the values for area and number of aggregates into intervals which are inversely proportional to the density of points, fit with Gaussian functions for each variable, and then integrated into a normalized two-dimensional distribution.

## RESULTS

Within 1 to 2 h, skin fibroblasts in culture come into close apposition to each other to form measurable networks, and after one day these networks degenerate and edges retract to leave behind aggregates (Supplementary Figure 2). Aggregates were investigated at 48 h using their average aggregate area per number. This method accurately diagnosed AD patients distinguishing them from AC and non-ADD (Fig. 1).

Two additional quantitative markers that measure the complexity of human skin fibroblast networks consisted of fractal dimension and lacunarity [30–33]. With these two measures, fractal and lacunarity curves were constructed at successive time points (Fig. 2). Recovery was measured by the slope and intercept of the fractal curves, and showed quantifiable differences for the three populations (AD, non-ADD, and AC). Lacunarity is a complementary measure for complexity discrimination that quantifies the gaps in the cellular networks. AD cell lines showed an increased average lacunarity when compared with cell lines from AC and non-ADD individuals. Finally, a fourth measure evaluated fibroblast migration after 48 h. This measure revealed a decreased number of migrating cells and rate of migration for AD and non-ADD fibroblasts. The last three methods offer the opportunity to screen not only AD from AC but also non-ADD such as Huntington's and Parkinson's diseases from the other two groups. These four methods complement each other and, as an internally consistent profile, offer a novel approach for diagnostic screening of AD patients.

*I: Average area per number of aggregates*

High accuracy was achieved when using the measure of the average area per number of aggregates. This measure was considerably higher for AD than for AC and non-ADD (Diagnostic accuracy 100%, $n = 33$ ($n_{AD} = 13$, $n_{AC} = 11$, and $n_{Non-ADD} = 9$ $p < 0.000001$ for AD versus AC, and $p < 0.00001$ for AD versus non-ADD).

The AD cells showed large isolated aggregates (Figs. 1A, 3A, Supplementary Figure 3A), while the AC and non-ADD fibroblasts showed numerous smaller aggregates (Figs. 1B, 3B). Similar results were obtained for 9 (5 AC, 4 AD) fresh samples from the clinic when tested with this method (green symbols in Fig. 1D).

The probability distribution of the cellular aggregates as a function of area and number at 48 h showed that the AD group ($n = 13$) separates well from the AC group ($n = 11$). The peak probability value for AD population is at ($N = 5$, Area = 12370) while the AC population has a peak at ($N = 8$, Area = 1004). The standard deviations for the AC population were $\sigma_N = 2.3$, $\sigma_{Area} = 451$, while for the AD population were $\sigma_N = 2.6$, $\sigma_{Area} = 5000$. These standard deviations indicated that the probability distributions for the numbers of aggregates had some overlap while the probability distributions for the areas had no overlap at half-width. Therefore, a simple method of increasing separability between AD and AC populations was to collapse the two variables into one by dividing them as area/number (see Materials and Methods section for details).

The population data (Fig. 1D) showed no overlap between AC, non-ADD, and AD. The average natural logarithm of area per number of aggregates increased linearly with AD duration (Fig. 1E), suggesting that this measure correlated with disease progression.

Thus far, the measures we have presented completely discriminate AD from AC and non-ADD leaving an uncertainty in separating AC from non-ADD. With the next three measures, we further refine the screening by addressing the question of separability of all three populations (AC, AD, and non-ADD).

*II: Fractal analysis*

The dynamics of spatiotemporal complexity such as network formation (Fig. 2A), network degeneration

(Fig. 2B), and recovery was measured by the fractal and lacunarity curves (Fig. 2C, E). The AD fibroblast networks measured by these physical parameters were markedly less complex when compared to AC and non-ADD networks. After network degeneration (~48 h, Fig. 2B), cells migrated and within a few days they approached confluence. This recovery was captured by a linear increase in fractal dimension (Fig. 2C). The slope versus the intercept of each curve that tracks fractal dimension as a function of time was markedly different in the three groups (97% accuracy, $n = 33$ ($n_{AD} = 13$, $n_{AC} = 10$, $n_{Non-ADD} = 9$); $p < 0.0001$ for AD versus AC, and $p < 0.00001$ for AD versus non-ADD). Thus, the fractal analysis was more powerful than the first method because it discriminates not only between AD and AC, non-ADD but also between AC and non-ADD ($p < 0.01$) (Fig. 2D).

*III: Lacunarity analysis*

Lacunarity is a complementary measure for fractal dimension used as a second level of complexity discrimination by quantifying the gaps of the fibroblast patterns. The average lacunarity of the fibroblasts was also higher for fibroblasts taken from AD when compared to AC and non-ADD fibroblasts. Typically, the lacunarity increased and peaked when the network degeneration was maximal, i.e., when only isolated aggregates were visible near the time point of 48 h (Fig. 2E, F). The lacunarity decreases as the network regeneration starts and the cells were becoming more confluent. The population data (Fig. 2F) showed that average lacunarity, like fractal analysis, discriminated not only between AD and AC, non-ADD but also between AC and non-ADD ($p < 0.01$) (Fig. 2F).

Unlike methods I and II, fractal and lacunarity analysis discriminated between the three groups (AC, non-ADD, and AD).

*IV: Cell migration*

Freely migrating cells were counted at 48 h, $N_1$, and approximately 7 h later, $N_2$. The migration rate was calculated as $R = (N_2 - N_1)/\Delta T$, where $\Delta T$ was the time interval between counts. A freely migrating cell was a cell that was not attached to the aggregates, as depicted by the green dots in Fig. 3A, B. The number of migrating cells was reduced in AD fibroblasts (Fig. 3A) when compared with AC (Fig. 3B). The population data (Fig. 3C) showed that AD fibroblasts (squares) and non-ADD fibroblasts (triangles) had a significantly lower number of migrating cells and rate of migration when compared with AC fibroblasts. AD fibroblasts (squares) showed the smallest number of migrating cells and the lowest migration rate, while AC fibroblasts (circles) showed the highest number of migrating cells and the highest migration rate. Interestingly non-ADD fibroblasts separated (with one exception) from AD and AC.

Importantly, the number of migrating cells decreased with increasing disease duration of AD (Fig. 3D).

*Effect of Aβ on network formation, cellular aggregation, and migration*

Initial experiments suggest that some of the differences between AD and AC fibroblasts were due to oligomerized Aβ. AC fibroblasts treated overnight with 1 μM oligomeric $A\beta_{1\text{-}42}$ changed their phenotype to AD-like phenotype when plated on 3-D matrix (Fig. 4A–D). Our preliminary results on AC cell lines ($n = 3$) showed that Aβ impairs network formation (Fig. 4B) by decreasing the network connectivity and increasing cellular aggregation at 48 h by increasing the size of cellular aggregates and by reducing the number of aggregates. The increased cellular aggregation was reflected in fractal and lacunarity curves which were AD-like (Fig. 4C, D). Aβ also impaired cellular migration in AC cell lines by reducing the number of migrating cells after 48 h. Interestingly, similar experiments on AD fibroblasts ($n = 3$) showed no distinguishable effect on cellular aggregation at 48 h, fractal dimension, and lacunarity. These findings were consistent with recently published results showing an excess of $A\beta_{1\text{-}40}$ in neurons derived from two familial and one sporadic AD skin fibroblast cell lines via induced pluripotent stem cells technology [37, 38].

The treatment with 1 μM oligomeric $A\beta_{1\text{-}42}$ in T25 flasks overnight did not result in cell death as indicated by the cell attachment on a 3-D matrix in the assay. Typically, for this assay, when the cells were platted on a 3-D matrix, within 30 min the viable cells attached and started forming network connections. Furthermore, the cell aggregation at 48 h (Fig. 4E, F) was another way of proving the cell viability.

*Accuracy, specificity, and sensitivity*

The methods described had an average rate of diagnostic accuracy of 97% (Supplementary Table 2) ranging between 95% for the average lacunarity and 100% for the average area per number of aggregates. For the fractal analysis (slope versus intercept), the

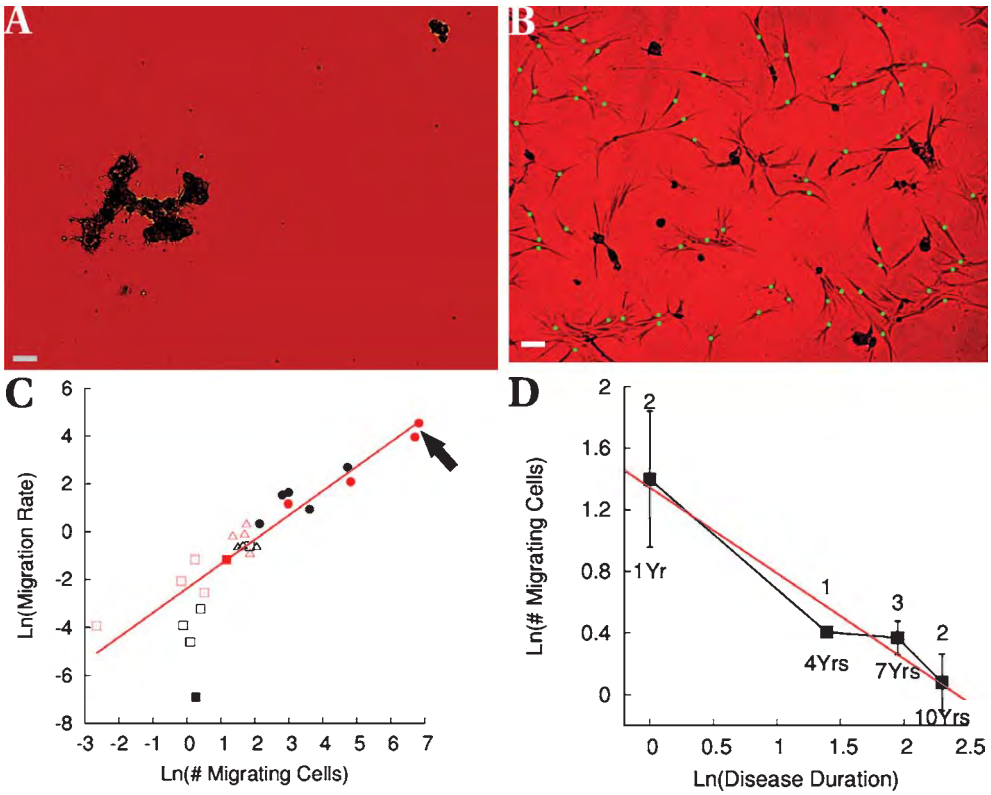


Fig. 3. Measure IV. Cell migration after 48 h. A) Examples of freely migrating fibroblasts marked with green dots in A (AD) and B (AC) at 48 h after plating. Scale bar is 10 μm. Examples of migrating cells pointed by the arrow in C. C) Natural logarithm of migration rate versus natural logarithm of number of migrating cells. Squares, AD ($n = 10$); triangles, non-ADD ($n = 7$); circles, AC ($n = 9$). Empty symbols were autopsy or genetic validation. Red symbols were double blind. D) Linear dependence (slope = −0.56, intercept = 1.34) of the natural logarithm of the number of migrating cells on the natural logarithm of AD disease duration. Error-bars are standard errors of the mean (SEM).

rate of success was 97%, while for the cell migration the rate of success was 96%. For the methods proposed, the average sensitivity was 98% (Supplementary Table 2) with a range between 92% for fractal analysis (95% confidence interval, 83% to 100%) and 100% for the average area per number of aggregates, lacunarity analysis, and cell migration.

The average sensitivity is 98%, while the average specificity is 98.5% (Supplementary Table 2). The two values different from 100% were measured for fractal analysis and cell migration which showed a sensitivity of 92% (sensitivity for fractal analysis: 95% confidence interval 83% to 100%), and a specificity of 94% (specificity for cell migration: 95% confidence interval 86% to 100%), respectively (Supplementary Table 2). Since the sample size was relatively small, the confidence intervals for these two values (sensitivity for fractal analysis and specificity for cell migration) were calculated step by step as described previously (http://www.wikihow.com/Calculate-95%25-Confidence-Interval-for-a-Test%27s-Sensitivity).

In summary, the four methods have an average accuracy of 97%, an average sensitivity of 98%, and an average specificity of 98.5%.

## DISCUSSION

A number of observations in the literature suggest that the extracellular matrix [28], membrane fluidity [23, 24], cytoskeletal protein expressions [25, 26], microtubule networks [29], and various interrelated signaling pathways including PKC, ERK [14–17], and calcium signaling [16] are altered in AD skin fibroblasts compared to AC cases. We hypothesized that all of these altered phenomena may have one biophysical read-out to distinguish AD skin fibroblasts with AC and non-ADD cases. This biophysical read-out tested here was the complex dynamical behavior of the skin fibroblasts in a 3-D matrix cell culture system. We intended to quantitatively measure the differences in network formation, cellular aggre-

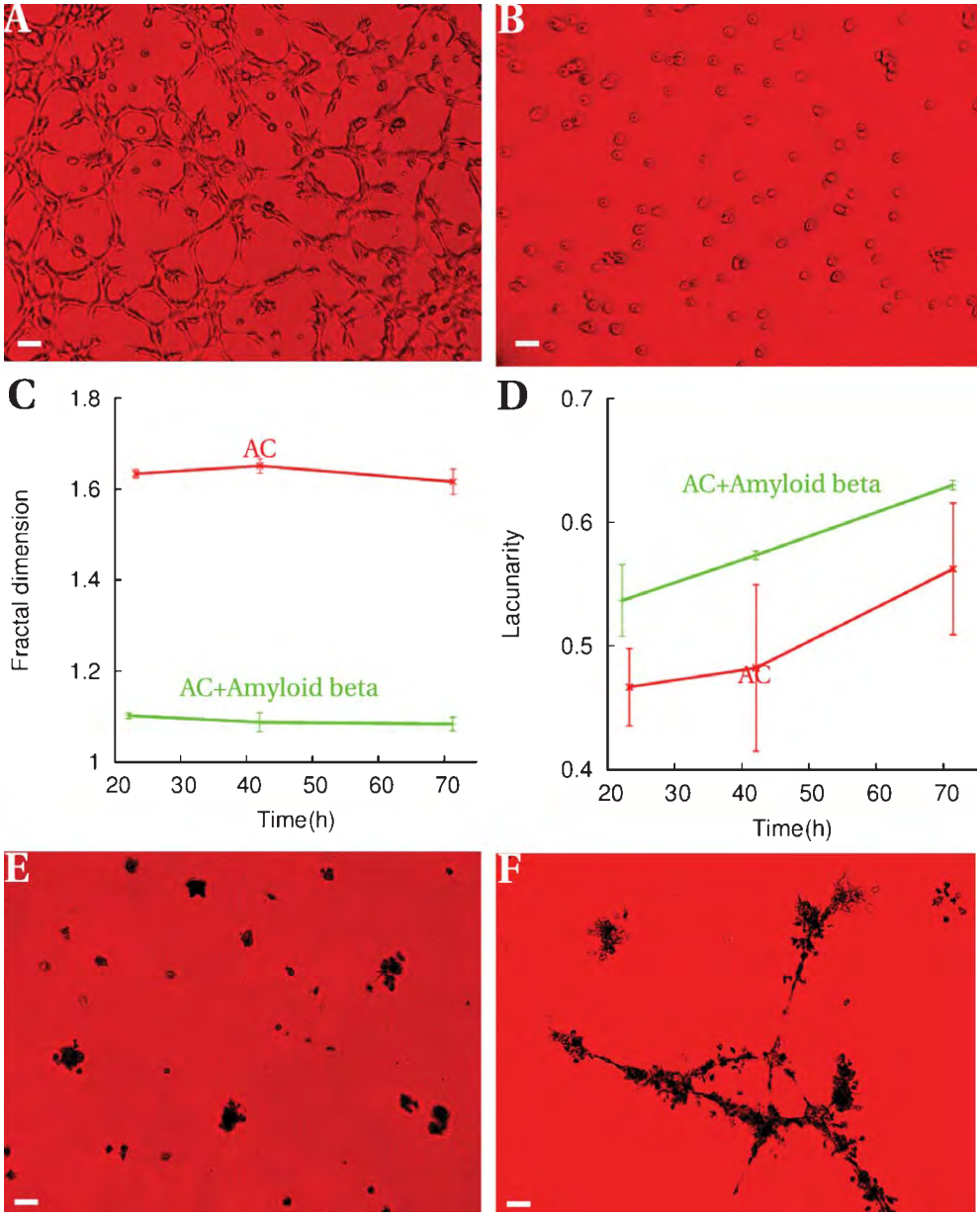


Fig. 4. Effect of Aβ on network formation and cellular aggregation. A) Control cell line at 2 and 0.5 h after plating on 3-D matrix. B). The same control cell line treated overnight with 1 μM oligomerized Aβ and visualized at 2 and 0.5 h showed impairment in network formation. C) Fractal dimension for the Aβ-treated control cell line (green) had an AD-like phenotype. D) Higher lacunarity for the Aβ-treated control cell line (green) was indicative of AD phenotype. E) Non-treated control cell line at 48 h after plating showing a typical high number of small aggregates. F) The same control cell line using $A\beta_{1\text{-}42}$ treated cells overnight showed at 48 h after plating a low number of large aggregates. Experiments depicted in E and F were done in parallel. Error-bars are standard error of the mean (SEM). Scale bar is 10 μm.

gation, and cell migration between AD, AC, and non-ADD.

During development, the ectoderm evolves into the skin, the sense organs, and the primitive nervous system. Increasing evidence has supported the so-called brain–skin axis [39, 40]. Mouse and human fibroblasts, for example, can be reprogrammed to become functional neurons with a combination of four transcription factors that mediate a pluripotent state [37, 38]. Therefore, the induced pluripotent stem cells technology can be used to induce neurons from skin fibroblasts and to further observe phenotypes relevant to AD. The

interaction between the cutaneous nervous system and skin cells participates in skin inflammation and wound healing [41]. Circadian clocks in peripheral skin fibroblasts are synchronized with the circadian pacemaker in the suprachiasmatic nucleus of the hypothalamus [42, 43]. Furthermore, there is evidence supporting a link between cutaneous (i.e., systemic) manifestations of abnormalities in amyloid metabolism and amyloid deposits in the brains of AD patients [39]. For example, presenilin-1 is one of the major components of the γ-secretase complex. Mutation of presenilin-1 increases the activity of the γ-secretase complex on the amyloid-β protein precursor and increases toxic Aβ production, which has been considered to be one of the major cause of AD [44, 45]. Presenilin-1 is also involved in epidermal growth factor receptor turnover [46]. Partial loss of presenilin-1 expression may lead to seborrheic keratoses and inflammatory skin diseases [47]. Gene expression studies using familial AD skin fibroblasts showed that the disease process may even start before the onset of cognitive decline [48]. Familial AD fibroblasts were found to produce excess Aβ in cultured fibroblasts [7, 8, 37].

A variety of molecular measures in skin fibroblasts indicated AD-specific deficits of PKC, and ERK 1/2 signaling, which are involved in the Aβ pathway [8, 15, 18, 19, 49]. This signaling has also been implicated in AD-specific deregulation of potassium channels [13] and electrical connections in fibroblasts grown in culture.

It is well known that $A\beta_{1\text{-}42}$ is more prone to aggregation than $A\beta_{1\text{-}40}$ and that its neurotoxicity is considered to be one of the main causes of neuronal damage. Prefibrillar aggregates of Aβ, but not mature fibrils, can impair cell viability when added to cell culture media [50]. From our own study [17–19], we did not find a significantly higher number of dead skin fibroblasts after 24 h of treatment with 1.0 μM $A\beta_{1\text{-}42}$ when compared with untreated cells. However, it seems likely that Aβ alone is not responsible for the diagnostic discrimination we see in skin fibroblasts. More likely, AD is a complex disease arising from the interaction of several imbalanced signaling pathways.

## CONCLUSIONS

The proposed four measures for screening of AD patients offer an exciting new opportunity to diagnose patients with a minimally invasive procedure. We found quantifiable differences in human skin fibroblast aggregation from AD patients when compared with AC and non-ADD patients. At 48 h, we used a quantitative measure, the average area per number of aggregates, change to "to separate AD from AC/non-ADD. The average area per number of aggregates appears to increase with AD duration, while the number of migrating cells appears to decrease with AD duration. We found that fractal and lacunarity curves, measuring the complexity of fibroblasts dynamics, show significant differences for the three groups.

Cell migration is impaired in diseased skin fibroblasts (AD/non-ADD) when compared with AC. The migration rate as a function of number of freely migrating cells shows non-overlapping clusters for AD, non-ADD, and AC. The average number of migrating cells is decreased with increasing duration of AD.

In conclusion, the four methods have a high accuracy (97%), a high sensitivity (98%), and are highly specific (98.5%). It is noteworthy that the Coriell Cell Repository samples were well characterized by independent diagnostic criteria (autopsy, clinical diagnostic, genetics of family history) and that these results have recently been replicated with a limited sample (4 AC, 5 AD) of fibroblasts taken from fresh biopsies. Thus, these results show promising potential to diagnostically screen AD from age-matched controls and non-Alzheimer's dementia.

## ACKNOWLEDGMENTS

We would like to thank Emily Reilly for counting the migrating cells in the 10× images under blind conditions. We would also like to thank Dr. Camilla Forssten from Alere Inc. for her ongoing valuable discussions and Alere Diagnostic for their alliance support. Finally, we would appreciate Dr. Shirley Neitch from Marshall University, Huntington, WV, for her oversight and the clinical diagnosis for the nine fresh samples presented in Fig. 1D.

Authors' disclosures available online (http://www.j-alz.com/disclosures/view.php?id=1462).

## REFERENCES

[1] Irizarry MC (2004) Biomarkers of Alzheimer disease in plasma. *NeuroRx* **1**, 226-234.

[2] Perry RH, Wilson ID, Bober MJ, Atack J, Blessed G, Tomlinson BE, Perry EK (1982) Plasma and erythrocyte acetylcholinesterase in senile dementia of Alzheimer type. *Lancet* **1**, 174-175.

[3] Eckert A, Cotman CW, Zerfass R, Hennerici M, Müller WE (1998) Lymphocytes as cell model to study apoptosis in Alzheimer's disease: Vulnerability to programmed cell death appears to be altered. *J Neural Transm Suppl* **54**, 259-267.

[4] Sevush S, Jy W, Horstman LL, Mao WW, Kolodny L, Ahn YS (1998) Platelet activation in Alzheimer disease. *Arch Neurol* **55**, 530-536.

[5] Sayer R, Law E, Connelly PJ, Breen KC (2004) Association of a salivary acetylcholinesterase with Alzheimer's disease and response to cholinesterase inhibitors. *Clin Biochem* **37**, 98-104.

[6] Bermejo-Pareja F, Antequera D, Vargas T, Molina JA, Carro E (2010) Saliva levels of Abeta1-42 as potential biomarker of Alzheimer's disease: A pilot study. *BMC Neurol* **10**, 108. doi:10.1186/1471-2377-10-108

[7] Soininen H, Syrjänen S, Heinonen O, Neittaanmäki H, Miettinen R, Paljärvi L, Syrjänen K, Beyreuther K, Riekkinen P (1992) Amyloid beta-protein deposition in skin of patients with dementia. *Lancet* **339**, 245-245.

[8] Citron M, Vigo-Pelfrey C, Teplow DB, Miller C, Schenk D, Johnston J, Winblad B, Venizelos N, Lannfelt L, Selkoe DJ (1994) Excessive production of amyloid beta-protein by peripheral cells of symptomatic and presymptomatic patients carrying the Swedish familial Alzheimer disease mutation. *Proc Natl Acad Sci U S A* **91**, 11993-11997.

[9] Johnston JA, Cowburn RF, Norgren S, Wiehager B, Venizelos N, Winblad B, Vigo-Pelfrey C, Schenk D, Lannfelt L, O'Neill C (1994) Increased beta-amyloid release and levels of amyloid precursor protein (APP) in fibroblast cell lines from family members with the Swedish Alzheimer's disease APP670/671 mutation. *FEBS Lett* **354**, 274-278.

[10] Scheuner D, Eckman C, Jensen M, Song X, Citron M, Suzuki N, Bird TD, Hardy J, Hutton M, Kukull W, Larson E, Levy-Lahad E, Viitanen M, Peskind E, Poorkaj P, Schellenberg G, Tanzi R, Wasco W, Lannfelt L, Selkoe D, Younkin S (1996) Secreted amyloid beta-protein similar to that in the senile plaques of Alzheimer's disease is increased *in vivo* by the presenilin 1 and 2 and APP mutations linked to familial Alzheimer's disease. *Nat Med* **2**, 864-870.

[11] Goldstein LE, Muffat JA, Cherny RA, Moir RD, Ericsson MH, Huang X, Mavros C, Coccia JA, Faget KY, Fitch KA, Masters CL, Tanzi RE, Chylack LT Jr, Bush AI (2003) Cytosolic beta-amyloid deposition and supranuclear cataracts in lenses from people with Alzheimer's disease. *Lancet* **361**, 1258-1265.

[12] Etcheberrigaray R, Ito E, Oka K, Tofel-Grehl B, Gibson GE, Alkon DL (1993) Potassium channel dysfunction in fibroblasts identifies patients with Alzheimer disease. *Proc Natl Acad Sci U S A* **90**, 8209-8213.

[13] Etcheberrigaray R, Ito E, Kim CS, Alkon DL (1994) Soluble beta-amyloid induction of Alzheimer's phenotype for human fibroblast K+ channels. *Science* **264**, 276-279.

[14] Govoni S, Bergamaschi S, Racchi M, Battaini F, Binetti G, Bianchetti A, Trabucchi M (1993) Cytosol protein kinase c downregulation in fibroblasts from Alzheimer's disease patients. *Neurology* **43**, 2581-2586.

[15] Favit A, Grimaldi M, Nelson TJ, Alkon DL (1998) Alzheimer's-specific effects of soluble β-amyloid on protein kinase C-α and -γ degradation in human fibroblasts. *Proc Natl Acad Sci U S A* **95**, 5562-5567.

[16] Ito E, Oka K, Etcheberrigaray R, Nelson TJ, McPhie DL, Tofel-Grehl B, Gibson GE, Alkon DL (1994) Internal Ca2+ mobilization is altered in fibroblasts from patients with Alzheimer disease. *Proc Natl Acad Sci U S A* **91**, 534-538.

[17] Zhao WQ, Ravindranath L, Mohamed AS, Zohar O, Chen CH, Lyketsos CG, Etcheberrigaray R, Alkon DL (2002) MAP kinase signaling cascade dysfunction specific to Alzheimer's disease in fibroblasts. *Neurobiol Dis* **11**, 166-183.

[18] Khan TK, Alkon DL (2006) An internally controlled peripheral biomarker for Alzheimer's disease: Erk1 and Erk2 responses to the inflammatory signal bradykinin. *Proc Natl Acad Sci U S A* **103**, 13202-13207.

[19] Khan TK, Nelson TJ, Verma VA, Wender PA, Alkon DL (2009) A cellular model of Alzheimer's disease therapeutic efficacy: PKC activation reverses Abeta-induced biomarker abnormality on cultured fibroblasts. *Neurobiol Dis* **34**, 332-339.

[20] Huang HM, Fowler C, Xu H, Zhang H, Gibson GE (2005) Mitochondrial function in fibroblasts with aging in culture and/or Alzheimer's disease. *Neurobiol Aging* **26**, 839-848.

[21] Humpel C (2011) Identifying and validating biomarkers for Alzheimer's disease. *Trends Biotechnol* **29**, 26-32.

[22] Mendonsa G, Dobrowolska J, Lin A, Vijairania P, Jong Y-JI, Baenziger NL (2009) Molecular profiling reveals diversity of stress signal transduction cascades in highly penetrant Alzheimer's disease human skin fibroblasts. *PLoS ONE* **4**, e4655.

[23] Zubenko GS, Wusylko M, Cohen BM, Boller F, Teply I (1987) Family study of platelet membrane fluidity in Alzheimer's disease. *Science* **238**, 539-542.

[24] Sims NR, Finegan JM, Blass JP (1987) Altered metabolic properties of cultured skin fibroblasts in Alzheimer's disease. *Ann Neurol* **21**, 451-457.

[25] Brandan E, Melo F, García M, Contreras M (1996) Significantly reduced expression of the proteoglycan decorin in Alzheimer's disease fibroblasts. *Clin Mol Pathol* **49**, M351-M356.

[26] Takeda M, Tatebayashi Y, Nishimura T (1992) Change in the cytoskeletal system in fibroblasts from patients with familial Alzheimer's disease. *Prog Neuropsychopharmacol Biol Psychiatry* **16**, 317-328.

[27] Uéda K, Cole G, Sundsmo M, Katzman R, Saitoh T (1989) Decreased adhesiveness of alzheimer's disease fibroblasts: Is amyloid β-protein precursor involved? *Ann Neurol* **25**, 246-251.

[28] Bellucci C, Lilli C, Baroni T, Parnetti L, Sorbi S, Emiliani C, Lumare E, Calabresi P, Balloni S, Bodo M (2007) Differences in extracellular matrix production and basic fibroblast growth factor response in skin fibroblasts from sporadic and familial Alzheimer's disease. *Mol Med* **13**, 542-550.

[29] Matsuyama SS, Jarvik LF (1993) Abnormal fibroblast microtubule response in familial Alzheimer disease. *Age* **16**, 152-158.

[30] Chirila FV, Rowland KC, Thompson JM, Spirou GA (2007) Development of gerbil medial superior olive: Integration of temporally delayed excitation and inhibition at physiological temperature. *J Physiol* **584**, 167-190.

[31] Pantic I, Harhaji-Trajkovic L, Pantovic A, Milosevic NT, Trajkovic V (2012) Changes in fractal dimension and lacunarity as early markers of UV-induced apoptosis. *J Theor Biol* **303**, 87-92.

[32] King RD, Brown B, Hwang M, Jeon T, George AT 9 (2010) Fractal dimension analysis of the cortical ribbon in mild Alzheimer's disease. *Neuroimage* **53**, 471-479.

[33] Gómez C, Mediavilla A, Hornero R, Abásolo D, Fernández A (2009) Use of the Higuchi's fractal dimension for the analysis of MEG recordings from Alzheimer's disease patients. *Med Eng Phys* **31**, 306-313.

[34] Hoshi M, Sato M, Matsumoto S, Noguchi A, Yasutake K, Yoshida N, Sato K (2003) Spherical aggregates of β-amyloid (amylospheroid) show high neurotoxicity and activate Tau protein kinase I/glycogen synthase kinase-3-beta. *Proc Natl Acad Sci U S A* **100**, 6370-6375.

[35] Noguchi A, Matsumura S, Dezawa M, Tada M, Yanazawa M, Ito A, Akioka M, Kikuchi S, Sato M, Ideno S, Noda M,

Fukunari A, Muramatsu S, Itokazu Y, Sato K, Takahashi H, Teplow DB, Nabeshima Y, Kakita A, Imahori K, Hoshi M (2009) Isolation and characterization of patient-derived, toxic, high mass amyloid β-protein (Aβ) assembly from Alzheimer disease brains. *J Biol Chem* **284**, 32895-32905.

[36] Sen A, Alkon DL, Nelson TJ (2012) Apolipoprotein E3 (ApoE3) but not ApoE4 protects against synaptic loss through increased expression of protein kinase C{epsilon}. *J Biol Chem* **287**, 15947-15958.

[37] Israel MA, Yuan SH, Bardy C, Reyna SM, Mu Y, Herrera C, Hefferan MP, Van Gorp S, Nazor KL, Boscolo FS, Carson CT, Laurent LC, Marsala M, Gage FH, Remes AM, Koo EH, Goldstein LS (2012) Probing sporadic and familial Alzheimer's disease using induced pluripotent stem cells. *Nature* **482**, 216-220.

[38] Vierbuchen T, Ostermeier A, Pang ZP, Kokubu Y, Südhof TC, Wernig M (2010) Direct conversion of fibroblasts to functional neurons by defined factors. *Nature* **463**, 1035-1041.

[39] Schreml S, Kaiser E, Landthaler M, Szeimies RM, Babilas P (2010) Amyloid in skin and brain: What's the link? *Exp Dermatol* **19**, 953-957.

[40] Zoumakis E, Kalantaridou SN, Chrousos GP (2007) The "brain-skin connection": Nerve growth factor-dependent pathways for stress-induced skin disorders. *J Mol Med* **85**, 1347-1349.

[41] Ansel JC, Kaynard AH, Armstrong CA, Olerud J, Bunnett N, Payan D (1996) Skin-nervous system interactions. *J Invest Dermatol* **106**, 198-204.

[42] Geyfman M, Andersen B (2009) How the skin can tell time. *J Invest Derm* **129**, 1063-1066.

[43] Tanioka M, Yamada H, Doi M, Bando H, Yamaguchi Y, Nishigori C, Okamura H (2009) Molecular clocks in mouse skin. *J Invest Derm* **129**, 1225-1231.

[44] Selkoe DJ (2001) Alzheimer's disease results from the cerebral accumulation and cytotoxicity of amyloid beta-protein. *J Alzheimers Dis* **3**, 75-80.

[45] Hardy J, Selkoe DJ (2002) The amyloid hypothesis of Alzheimer's disease: Progress and problems on the road to therapeutics. *Science* **297**, 353-356.

[46] Repetto E, Yoon IS, Zheng H, Kang DE (2007) Presenilin 1 regulates epidermal growth factor receptor turnover and signaling in the endosomal-lysosomal pathway. *J Biol Chem* **282**, 31504-310516.

[47] Tournoy J, Bossuyt X, Snellinx A, Regent M, Garmyn M, Serneels L, Saftig P, Craessaerts K, De Strooper B, Hartmann D (2004) Partial loss of presenilins causes seborrheic keratosis and autoimmune disease in mice. *Hum Mol Genet* **13**, 1321-1331.

[48] Nagasaka Y, Dillner K, Ebise H, Teramoto R, Nakagawa H, Lilius L, Axelman K, Forsell C, Ito A, Winblad B, Kimura T, Graff C (2005) A unique gene expression signature discriminates familial Alzheimer's disease mutation carriers from their wild-type siblings. *Proc Natl Acad Sci U S A* **102**, 14854-14859.

[49] Etcheberrigaray R, Tan M, Dewachter I, Kuipéri C, Van der Auwera I, Wera S, Qiao L, Bank B, Nelson TJ, Kozikowski AP, Van Leuven F, Alkon DL (2004) Therapeutic effects of PKC activators in Alzheimer's disease transgenic mice. *Proc Natl Acad Sci U S A* **101**, 11141-11146.

[50] Cecchi C, Fiorillo C, Baglioni S, Pensalfini A, Bagnoli S, Nacmias B, Sorbi S, Nosi D, Relini A, Liguri G (2007) Increased susceptibility to amyloid toxicity in familial Alzheimer's fibroblasts. *Neurobiol Aging* **28**, 863-876.